INTERNATIONAL JOURNAL FOR NUMERICAL METHODS IN FLUIDS
Int. J. Numer. Meth. Fluids 2003; **42**:1321–1343 (DOI: 10.1002/fld.587)

Evaluation of one- and two-equation low-*Re* turbulence models. Part II—Vortex-generator jet and diffusing S-duct flows

M. I. Yaras*,†,‡ and A. D. Grosvenor§

Department of Mechanical and Aerospace Engineering, Carleton University, Ottawa, Ont., Canada K1S 5B6

SUMMARY

This second segment of the two-part paper systematically examines several turbulence models in the context of two flows, namely a vortex flow created by an inclined jet in crossflow, and the flow field in a diffusing S-shaped duct. The test cases are chosen on the basis of availability of high-quality and detailed experimental data. The tested turbulence models are integrated to solid surfaces and consist of: Rodi's two-layer k–ε model, Wilcox's k–ω model, Menter's two-equation shear–stress-transport model, and the one-equation model of Spalart and Allmaras. The objective of the study is to establish the prediction accuracy of these turbulence models with respect to three-dimensional separated flows with streamline curvature. At the same time, the study establishes the minimum spatial resolution requirements for each of these turbulence closures, and identifies the proper low-Mach-number preconditioning and artificial diffusion settings of a Reynolds-averaged Navier–Stokes algorithm for optimum rate of convergence and minimum adverse impact on prediction accuracy. Copyright © 2003 John Wiley & Sons, Ltd.

KEY WORDS: low-Re turbulence modelling; vortex-generator inclined jets; diffusing S-ducts

1. INTRODUCTION

This paper extends the evaluation of several one- and two-equation turbulence models contained in Part 1 of this study to include three-dimensional separated flows. In light of the performance of the turbulence models for the simpler flows of Part 1, only four of the five turbulence models in question are considered here. These are: the two-layer k–ε model of Rodi and his co-workers [1], the k–ω model of Wilcox [2], the two-equation shear–stress-transport model of Menter [3], and the one-equation eddy-viscosity model of Spalart and Allmaras [4]. The evaluation of these models is based on a vortex-generator-jet flow [5] and the flow in a

*Correspondence to: M. I. Yaras, Department of Mechanical and Aerospace Engineering, Carleton University, 1125 Colonel By Drive, Ottawa, Ont., Canada K1S 5B6.
†E-mail: metin-yaras@carleton.ca
‡Associate Professor.
§Graduate Student.

Contract/grant sponsor: National Research Council of Canada; contract/grant number: 31184-8-8847/001/ST

Received 3 November 2000
Revised 21 April 2003

diffusing S-duct [6]. These flows were chosen on the basis of availability of detailed, high-quality measurements, and the extent of challenging flow features such as three-dimensional boundary layers, three-dimensional flow separation/reattachment and vortical flows.

2. SIMULATIONS OF A VORTEX-GENERATOR-JET FLOW

This section presents vortex-generator jet (VGJ) predictions for Findlay's [5] vectored-jet-in-crossflow experiment. Findlay tested several combinations of θ (skew angle) and Φ (pitch angle). The configuration that is chosen as a test case ($\theta = -90°, \Phi = 30°$) is not optimum with respect to boundary-layer control. Nonetheless, this configuration was chosen since the resultant turbulence levels in the wake of the jet were significantly higher than for the remaining configurations.

Streamwise vortices generated by the VGJs are the key mechanisms in providing manipulation of the local flow field. In this respect, it is particularly important to accurately predict the cross-stream transport of momentum facilitated by these vortices which, in turn, requires precise prediction of their streamwise trajectory, concentration and diffusion rates. Therefore, the analysis of simulation results presented herein focuses on these aspects of the VGJ flow field.

2.1. Computational domain, boundary conditions and iteration parameters

The simulated jet, depicted schematically in Figure 1, has an exit-plane cross-section of $1D \times 2D$. The jet Reynolds number, Re_D, based on the area-averaged jet velocity is 4910, and the jet-to-crossflow velocity ratio (VR) is 1.5. The crossflow freestream velocity is 3.84 m/s, and at the upstream end of the computational domain in the crossflow direction ($x = -5D$), the boundary layer that had developed under zero pressure gradient reaches $Re_\theta = 445$. The computational domain was chosen to extend $5D$ upstream of the jet exit, such that the inflow boundary remained unaffected by the jet flow field, and $11D$ in the downstream direction to include the flow region for which experimental data was available. The lateral extent of the computational domain was based on the spacing of the multiple jets in Findlay's experiments ($= 3D$), and periodic conditions were specified at the side boundaries.

At the top outflow boundary, located at $z/D = 7$, static pressure with a uniform distribution was specified and all other quantities were extrapolated from within the domain. It was also attempted to fix the static pressure at only a single node at this boundary and match the cross-stream pressure gradients in the plane of the boundary to those in the adjacent interior grid plane. However, this adversely affected the rate of convergence to a solution. Specification of uniform pressure required the top boundary to be placed sufficiently above the jet exit to prevent it from interfering with the natural development of vortex roll-up and subsequent diffusion. Several locations were considered for this boundary to establish sensitivity of the predicted flow field to the size of the computational domain. Upon setting the pressure at the top outflow boundary, no pressure specification was required at the aft outflow boundary located at $x/D = 11$.

The freestream velocity at the inflow boundary for the crossflow ($x = -5D$) was set to 3.84 m/s as per Findlay's experimental conditions. The flow direction was aligned with the x-axis and the turbulence parameters were set to: $k = 1.3 \times 10^{-3}$, $\varepsilon = 7$ for Rodi's k–ε model;

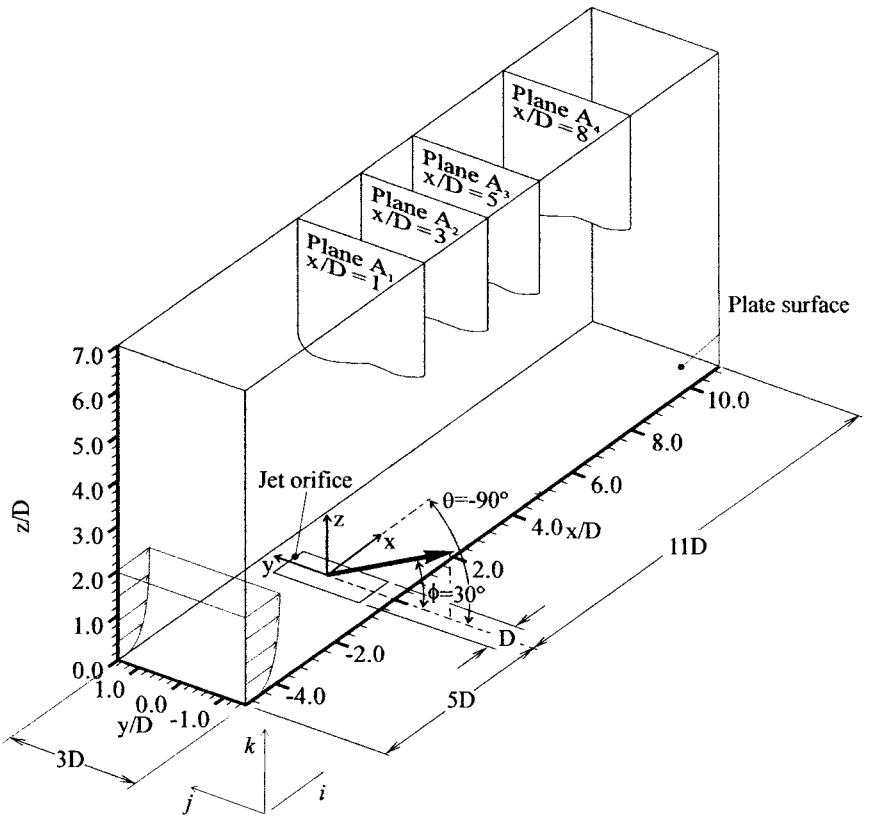

Figure 1. Computational domain for the VGJ.

$k=1.8\times10^{-6}$, $\omega=100$ for the k–ω and SST models; and $\chi=0.77$ for the SA model. The profiles of velocity and k in the crossflow boundary layer ($Re_\theta=445, \delta\approx 2D$) were obtained from polynomial curve fits to the experimental data, and the remaining turbulence properties (ε, ω and χ) were obtained from separately performed flat-plate turbulent boundary-layer simulations.

The remaining boundary condition that requires some consideration is the inflow boundary for the jet. It is well known that the distributions of velocity and turbulence quantities at this boundary are generally far from being uniform. A number of simulation studies have included in the computational domain the pipe leading to the jet-exit plane [7, 8], and even the plenum feeding the pipe. There have also been studies that completely ignored the non-uniformity of the flow at the jet-exit plane [9–11].

In the context of industrial calculations involving multiple VGJs, inclusion of jet pipes, and possibly plenums feeding these pipes, into the computational domain is undesirable since its impact on computational times would be significant. In the present simulations, the jet inflow boundary conditions were specified right at the exit plane of the jet. The ultimate objective was to simply impose uniform flow conditions at this inflow boundary, as has been done by several other researchers. To justify this approach, simulations were also performed

with non-uniform flow at the jet-exit plane for comparison. For these non-uniform conditions, polynomial chi-square surface fits were performed to the velocity magnitude, flow direction and turbulence kinetic energy data of Findlay [5]. These polynomial approximations had to be implemented in patches to ensure reasonable agreement with the experimental data. Figure 2 shows the extent of flow non-uniformity at the jet exit plane, and the polynomial surface fits used in the simulations.

Surface fits for flow direction were of similar quality, and are not shown here since the variation in flow direction was small (less than 10°). For simulations with uniform flow conditions at the jet exit plane, average values of velocity magnitude, direction and turbulence kinetic energies were used. Variation of ε in the jet-exit plane was determined using

$$\varepsilon = \frac{k^{3/2}}{0.2D_{\mathrm{h}}} \tag{1}$$

from which distributions of ω and $\tilde{\nu}_{\mathrm{e}}$ could be readily calculated.

For optimum rates of convergence, the artificial compressibility parameter, c/a, was set to $\max[3.0\ \mathrm{m/s}; 2.0V_{\mathrm{local}}]$, while the convective and diffusive time-step limits were determined on the basis of $K_{\mathrm{c}} = 1.8$, $K_{\mathrm{d}} = 0.1$. The artificial dissipation parameter, κ_4, was set to 0.005. Initial and lower threshold settings of the turbulence parameters k, ε, ω and χ, were also the same as those used in the test cases presented in Part 1. For Rodi's k–ε model, the turbulence production-to-destruction ratio of $(\mathscr{P}_k/\mathscr{D}_k)$ had to be limited to 20 to prevent divergence of the solution. The unbounded growth of this ratio tended to take place in the shear layer between the jet and crossflow, upstream of the roll-up process.

2.2. *Computational grid*

In identifying the optimum grid configuration, a series of grids were chosen that systematically provided local refinement in selected portions of the computational domain where spatial gradients in the flow field were relatively high. Specifically, emphasis was placed on establishing sufficient resolution in the vorticity field downstream of the jet orifice, in the core region of the jet, and along the perimeter of the jet. In proximity of the wall surface ($z/D = 0.0$), resolution in the z direction was fixed based on the requirement of $z_1^+ = 1.25$ and a minimum of 15 nodes in the boundary layer, established in the test cases of Part 1 to be adequate for all of the turbulence models in question. In addition to the node count, locations of the top and aft outflow boundaries were also varied to establish sensitivity of the predicted flow to the size of the computational domain. The ultimate objective of such a node-count and domain-size-optimization exercise is to identify the best combination of these parameters that would allow accurate prediction of the VGJ flow in the shortest time. It must be mentioned that the current optimization is specific to the VGJ configuration being considered with respect to θ, Φ, VR and lateral jet spacing. Nonetheless, it should be possible to extrapolate from the present results to establish first-order estimates of minimum grid and domain size requirements of alternative VGJ configurations.

The tested grid and computational-domain-size combinations are summarized in Table I, and are displayed in Figure 3. Between these grids, the maximum variations in the local

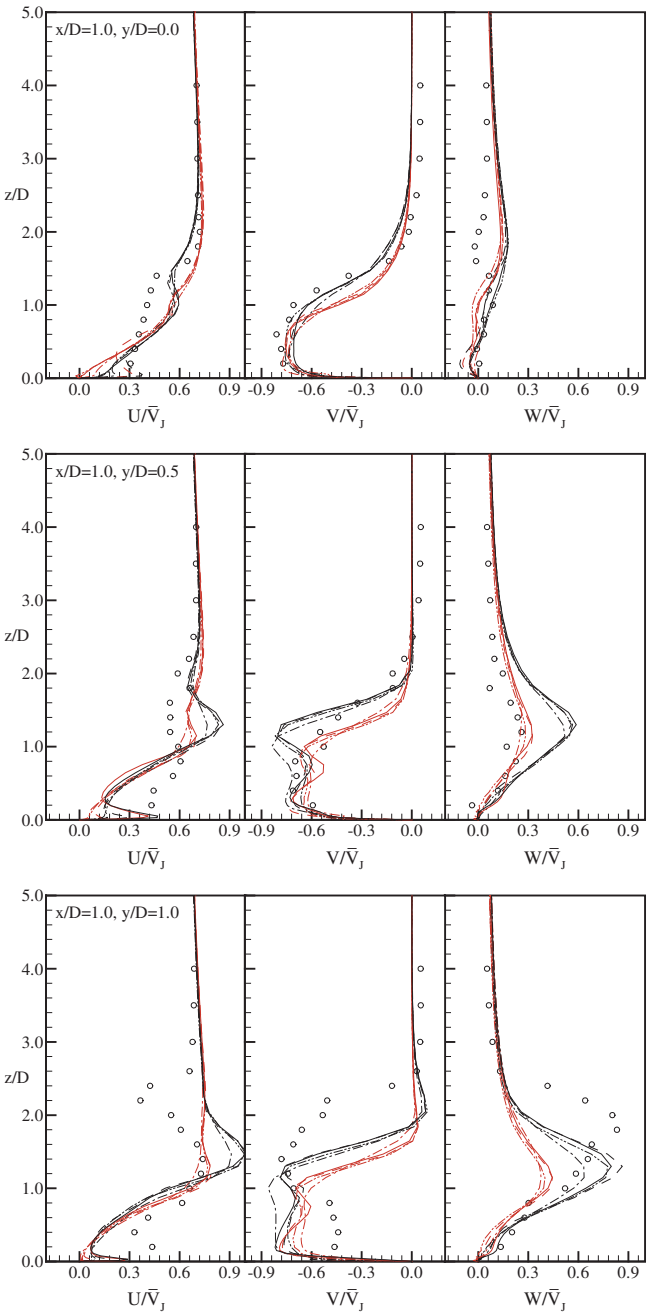

Plate 1. Comparison of predicted velocity profiles in plane A_1 with experimental data: sensitivity to turbulence models and jet boundary condition. ○, Findlay's expt. (1998); - - -, SA model; -·-·-, Rodi's k–ε model; ···, k–ω model; —, Menter's SST model. (Red curves: uniform jet-exit flow; black curves: non-uniform jet-exit flow).

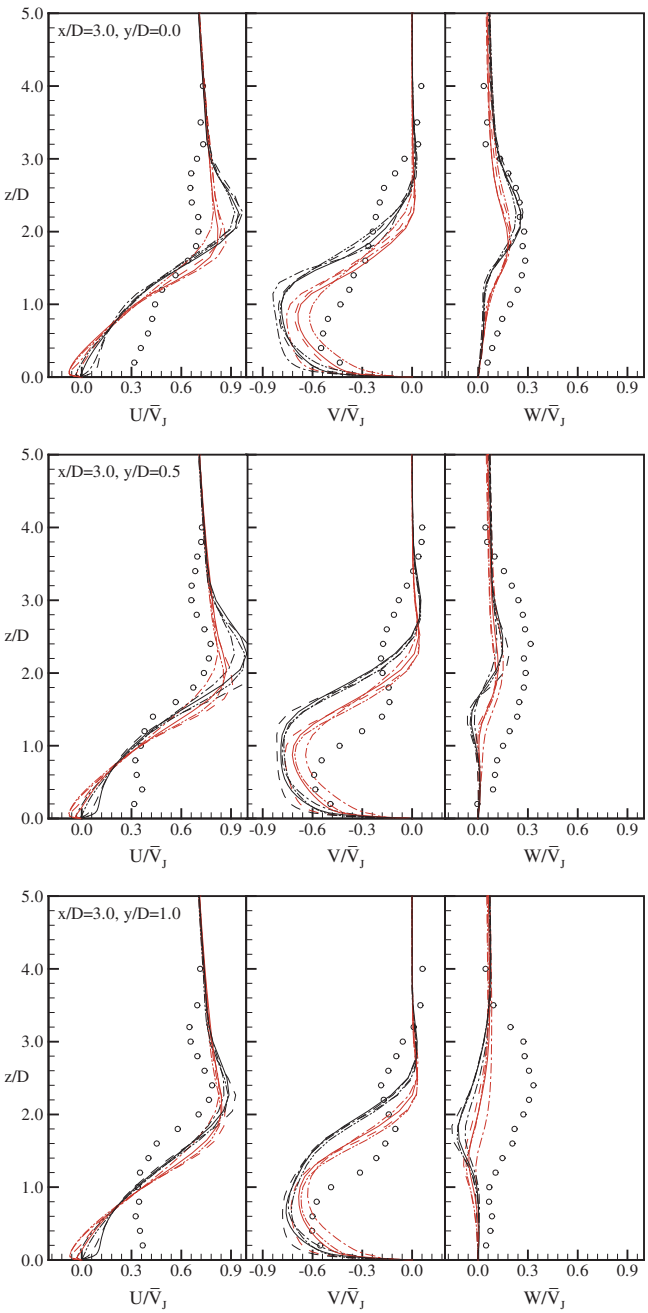

Plate 2. Comparison of predicted velocity profiles in plane A_2 with experimental data: sensitivity to turbulence models and jet boundary condition. ○, Findlay's expt. (1998); - - -, SA model; - · - · -, Rodi's k–ε model; - · · · · · · · -, k–ω model; —, Menter's SST model. (Red curves: uniform jet-exit flow; black curves: nonuniform jet-exit flow).

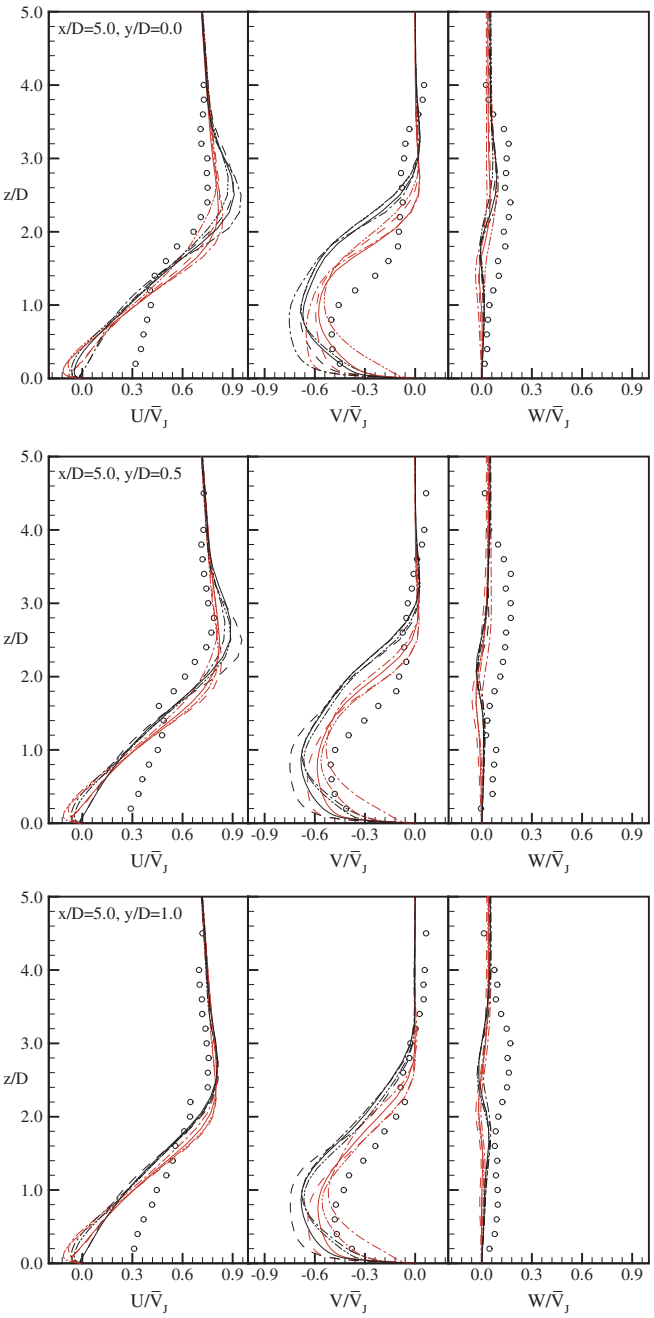

Plate 3. Comparison of predicted velocity profiles in plane A_3 with experimental data: sensitivity to turbulence models and jet boundary condition: ○, Findlay's expt. (1998); - - -, SA model; -·-·-, Rodi's k–ε model; ·····, k–ω model;—, Menter's SST model. (Red curves: uniform jet-exit flow; black curves: non-uniform jet-exit flow).

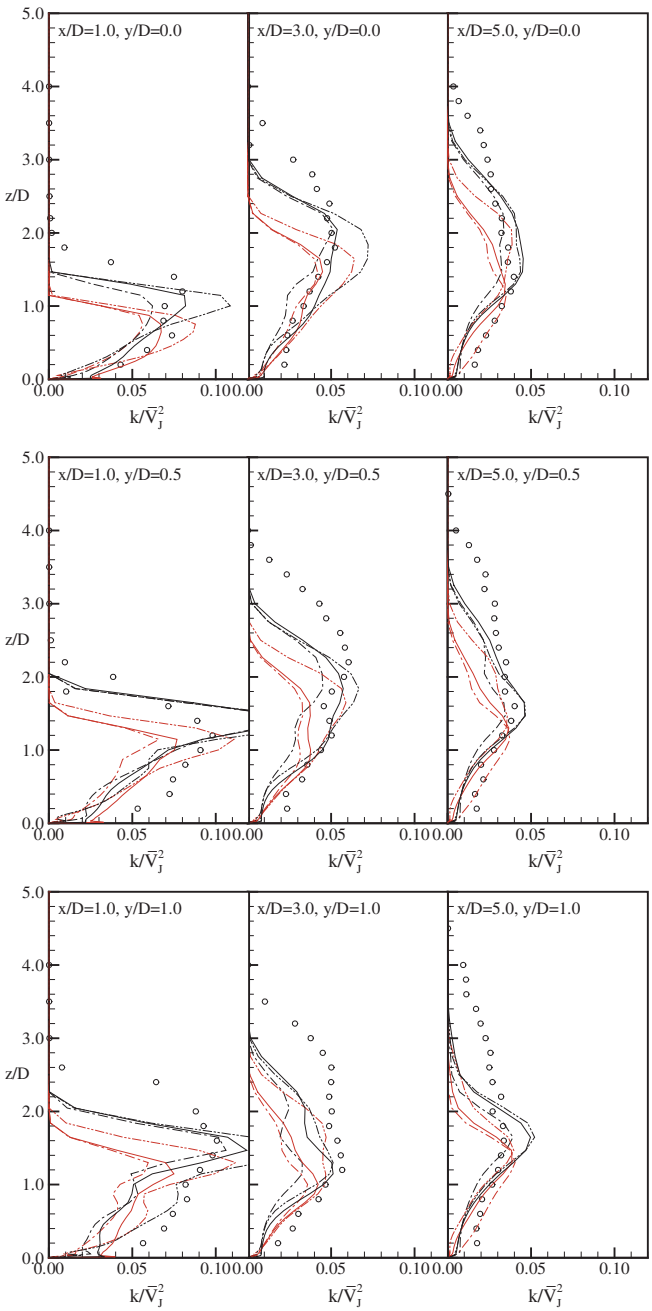

Plate 4. Comparison of predicted k profiles (planes A_1–A_3) with experimental data: sensitivity to turbulence models and jet boundary condition: ○, Findlay's expt. (1998); - - - -, Rodi's k–ε model; - ·· - ·· - ·· -, k–ω model; —, Menter's SST model. (Red curves: uniform jet-exit flow; black curves: non-uniform jet-exit flow).

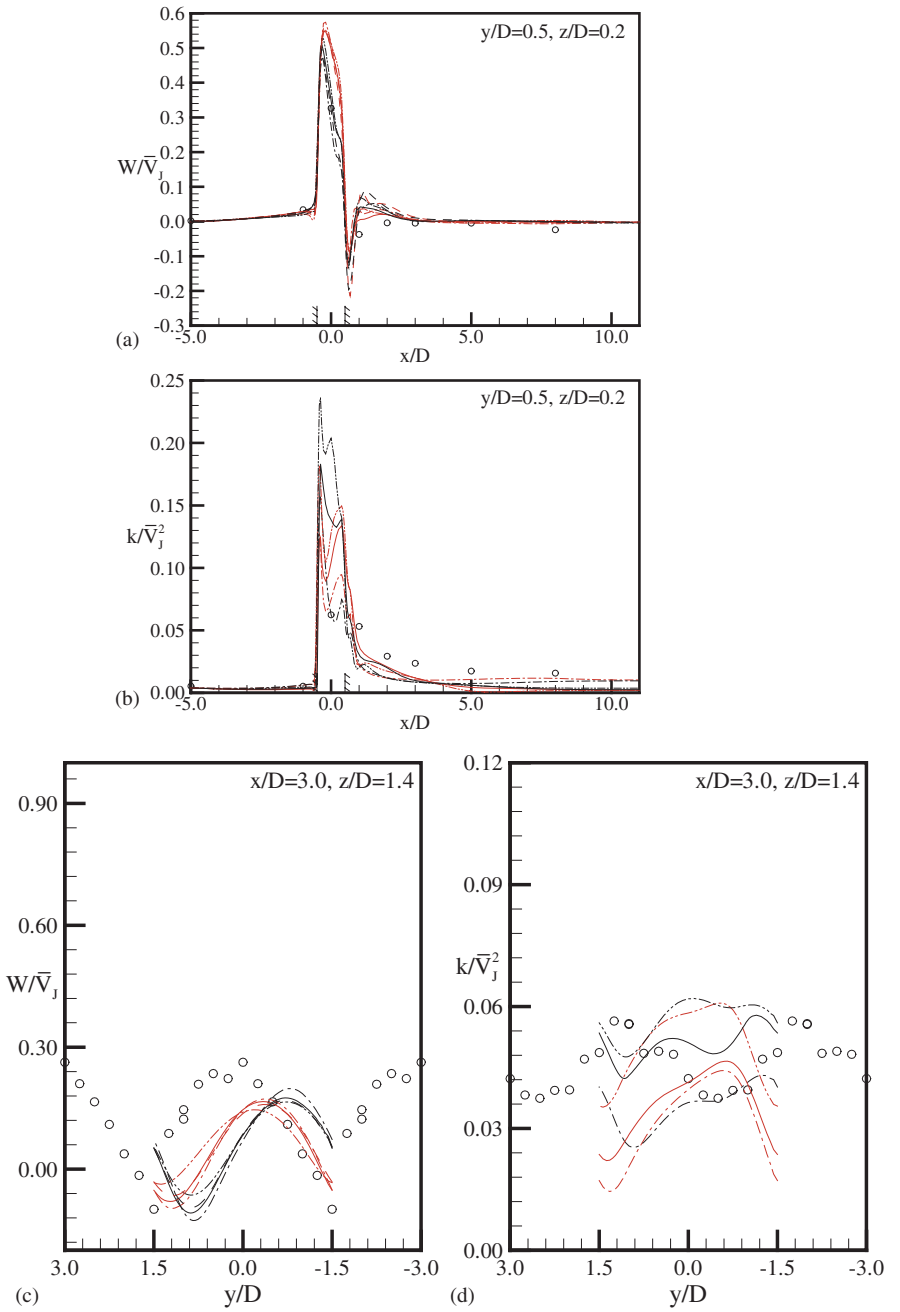

Plate 5. Comparison of predicted velocity and k profiles with experimental data: (a) W and (b) k across shear layer; (c) W and (d) k across streamwise vorticity field—sensitivity to turbulence models and jet boundary condition. ○, Findlay's expt. (1998); - - -, SA model; -·-·-, Rodi's k–ε model; -·-·-·-·-, k–ω model; —, Menter's SST model. (Red curves: uniform jet-exit flow; black curves: nonuniform jet-exit flow).

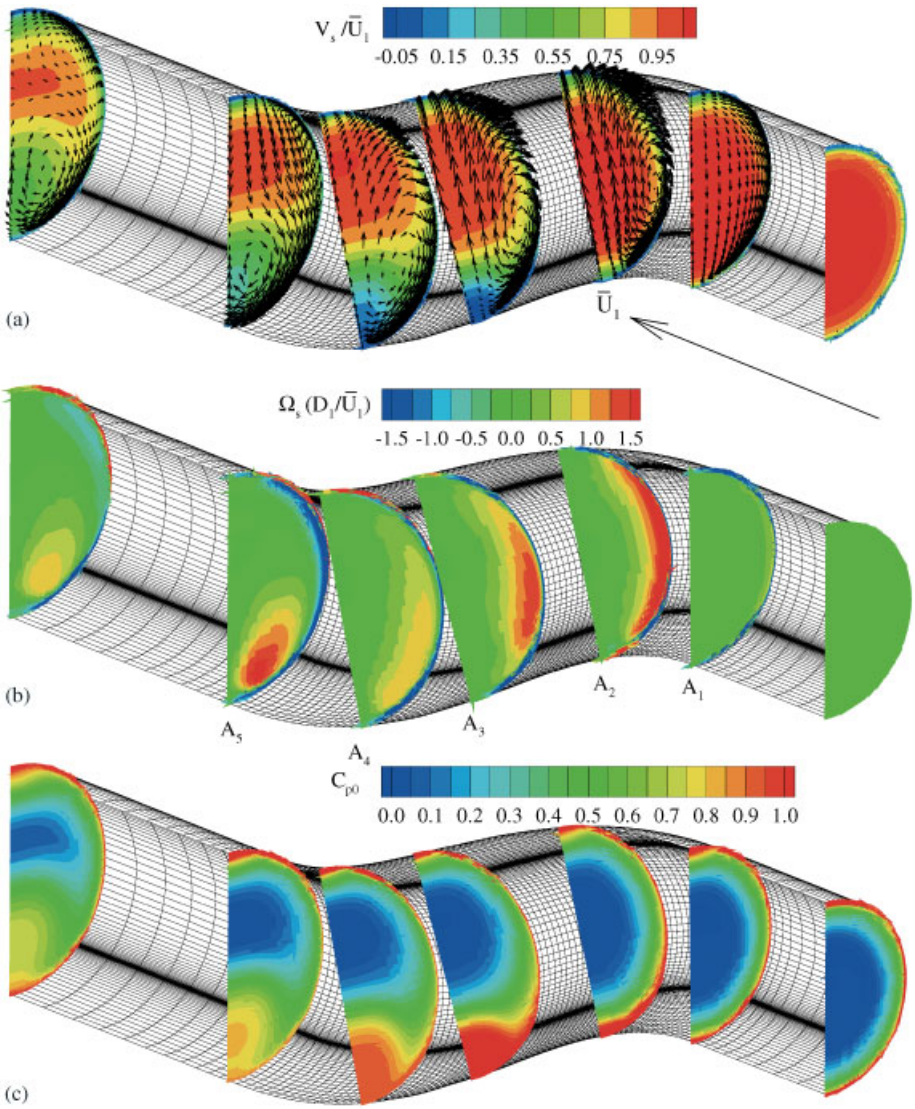

Plate 6. M2129 diffusing S-duct flow predicted with the SA model: (a) streamwise velocity, (b) streamwise vorticity and (c) total pressure.

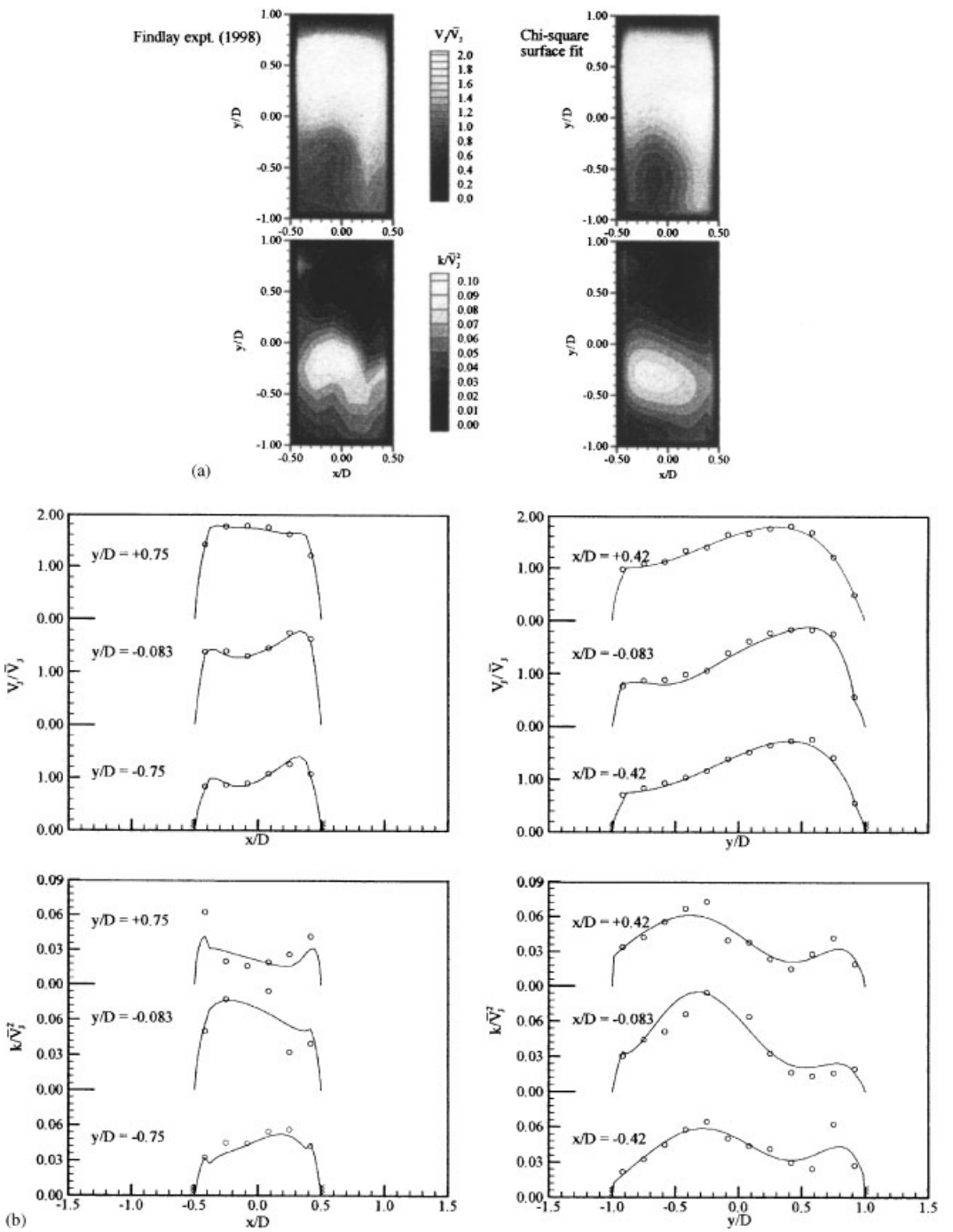

Figure 2. Distributions of V_J and k at the jet exit plane: ○, Findlay expt. (1998); —, surface fit.

Table I. Grid details for the VGJ simulations.

Grid	N_i	N_j	N_k	Number of nodes in: Inflow boundary layer	Jet core*	Jet shear layer*	Largest grid cell	Top outflow (z/D)	Aft outflow (x/D)
A	47	37	29	20	11	7	$1D$	5	8
B	59	37	29	20	9	5	$1/2D$	5	8
C	65	37	43	20	9	5	$1/2D$	7	11
D	69	61	43	20	15	9	$3/4D$	7	11

*These node counts relate to flow region just above the jet orifice.

velocity components were within about 6% of $\bar{V}_J$, whereas k, and Ω_x varied within about 5% of the maximum values encountered in the computational domain.

Since the amount of artificial dissipation affecting the solution is related to the spatial resolution, it is essential that any grid optimization study be performed in this context. Simulations were thus performed with values of 0.005 and 0.01 for κ_4, the scaling factor for fourth-order-difference artificial dissipation. On the coarsest grid considered, the sensitivity to κ_4 was about 2.5% of $\bar{V}_J$ for the local velocity components, 6% for k and 3.5% for Ω_x with respect to their maximum values within the computational domain. This sensitivity was significantly less on Grid D.

Based on these sensitivity analyses, Grid A can be judged to be adequate for computations that are time critical in an industrial setting. However, to maximize the accuracy in the comparisons of turbulence models and alternative considerations of jet-exit boundary conditions presented herein, the simulations were based on the more conservative spatial resolution and domain size of Grid D.

2.3. *Description of flow physics*

Prior to discussions of prediction sensitivity to the choice of grid, boundary conditions and turbulence models, a typical set of results of these simulations is presented here to examine the physics of the flow. The main features of the VGJ flow field predicted with Menter's SST model are depicted in Figure 4. The velocity, streamwise vorticity (Ω_x), and turbulence kinetic energy (k) fields, as well as the surface C_f distribution in the near field of the jet, accompanied by streamlines at the first set of nodes off the wall, are displayed.

A significant spanwise velocity component, with peak magnitudes comparable to the initial jet velocity, is observed to persist as far as $8D$ downstream of the jet orifice, which is the result of the shallow pitch angle and spanwise orientation of the jet combined with the relatively large jet-to-crossflow velocity ratio. A single dominant streamwise vortex is noted to develop, but is observed to be relatively weak to start with, and loses its strength rapidly with downstream distance. Presence of this vortex, in conjunction with the small initial pitch angle of the jet, are most likely responsible for the collective reorientation of the cross-stream velocity component from the initial 30° towards 0° within about $1.5D$ downstream distance. Before studying the crossflow velocity and streamwise vorticity distributions further, examination of the vector field topology (Figure 4d) should help to shed light on the overall flow development.

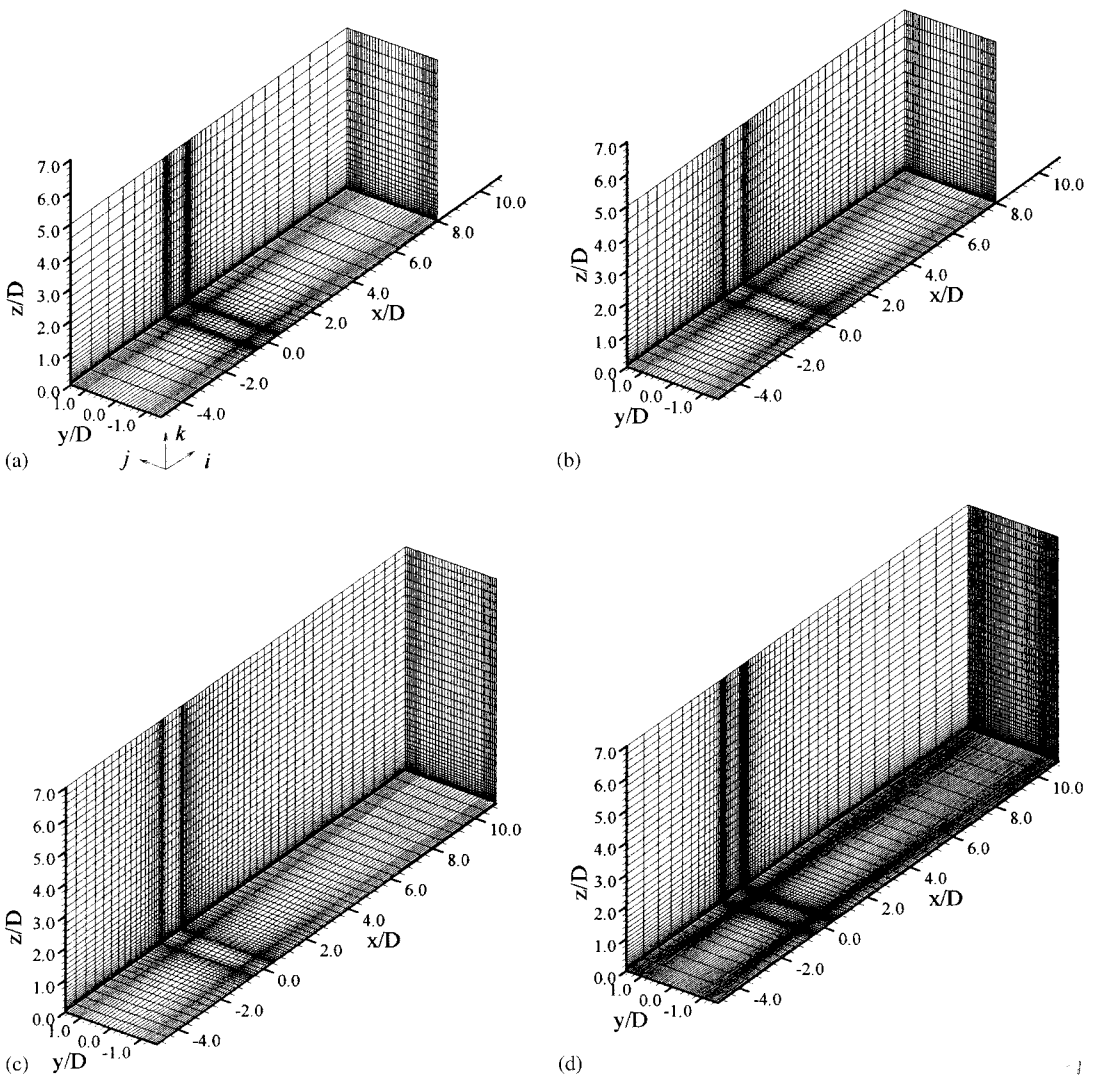

Figure 3. Node distributions for the VGJ simulations.

The stagnation point in front of the jet is indicated by the saddle of separation Ss1. The location of this point is biased toward the negative y direction relative to the centre of the jet orifice due to the large jet skew angle. The same trend was observed by Barberopoulos and Garry [12] for a jet at 60° skew angle. Negative bifurcation lines (NBL1, 2), or three-dimensional lines of separation, extend out from Ss1 in the negative and positive y directions providing an indication of the extent of the separated (recirculating) region in front of the jet. Due to the close proximity of the adjacent jets in the present test case, both of the NBLs lead into separation saddles (Ss2) at the jet orifice. Thus, instead of wrapping around the jet and augmenting focus nodes Fl and F2, as is the case for a single jet [12], the NBLs are

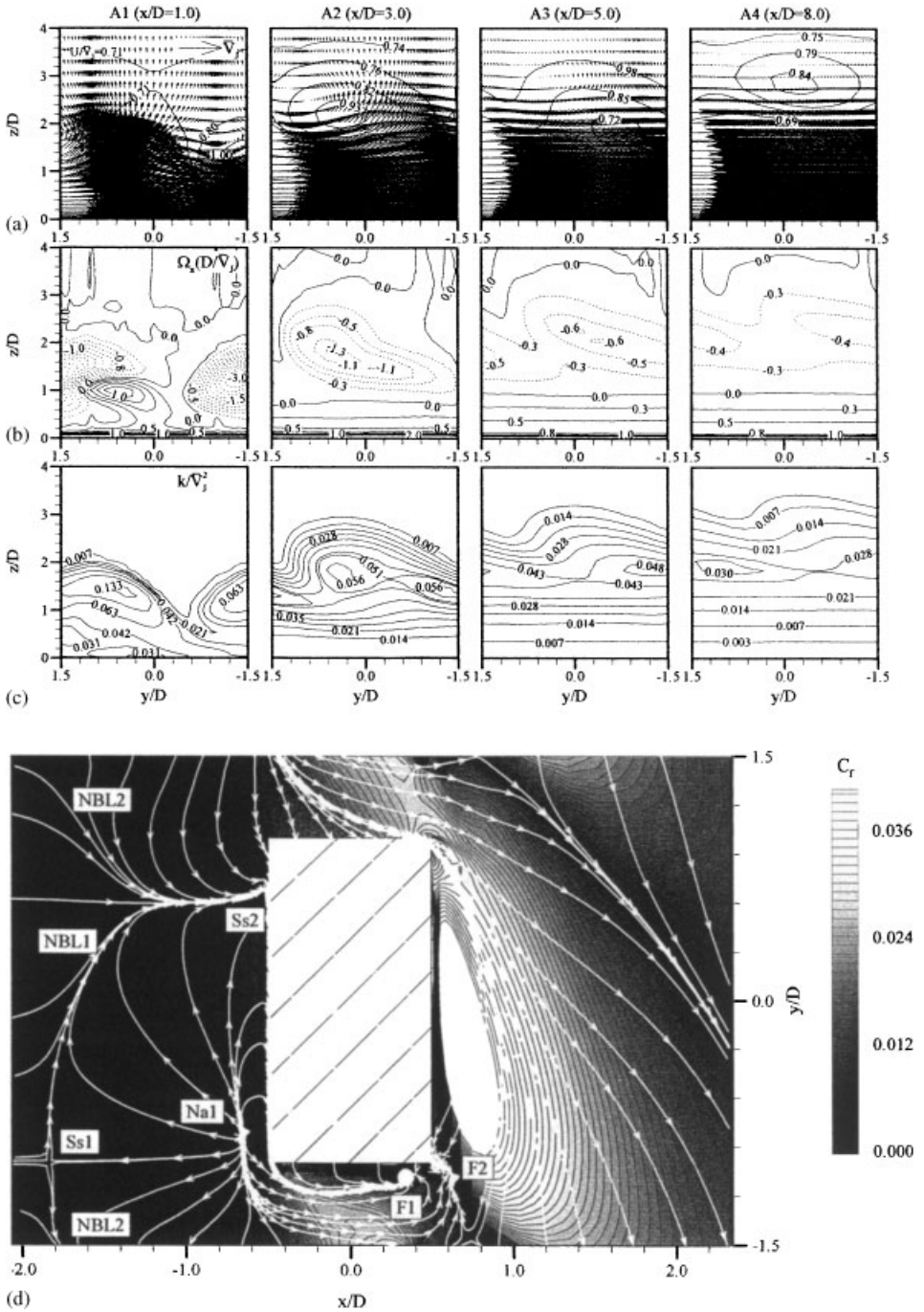

Figure 4. Features of the VGJ flowfield, based on Menter's SST model: (a) Cross-flow velocity vectors (V, W) and U contours, (b) Ω_x contours (negative values indicated by dashed lines), (c) k contours and (d) C_f and streamlines at first node off the wall.

blocked. This would be expected to produce a weaker streamwise vortex behind the orifice and also explains why horseshoe vortices cannot be discerned from the velocity or vorticity plots downstream of the jet orifice.

A node of attachment (Na1) follows Ss1 and feeds two focus nodes of separation (F1 and F2) at the corner $x/D = 0.5, y/D = 1.0$, which constitute the starting point of the dominant streamwise vortex. The close proximity of the two focus nodes to each other is due to the high skew angle of the present jet. This pattern has also been observed by Barberopoulos and Garry [12] for their jet at 60° skew.

Having identified the origin of the dominant streamwise vortex from the surface vector topology, the remaining details of the vortex development can be discerned from parts (a)–(c) of Figure 4. At plane A_1, the negative vorticity field associated with this vortex is seen to be partially annihilated on the upwash side by positive vorticity convected away from the boundary layer. Further downstream, in planes A_2, A_3 and A_4, this partially annihilated region is noted to contribute to the spanwise smearing of the negative vorticity field as it rotates and stretches. This smearing effect, in turn, is reflected in the cross-stream distribution of k. These observations are supported by the results of Khan [13] who noted lower vorticity magnitudes and higher deformation of the vorticity field at a skew angle (θ) of 90° compared to $\theta = 60°$, the latter of which he deemed to be the optimum value for boundary layer control at $\Phi = 30°$ and VR = 1.0.

2.4. Simulation results

Prediction results for the four turbulence models in question are shown in Figures 5–6 and Plates 1–5. The value of maximum streamwise vorticity, displayed in Figure 5(a), is predicted reasonably well with Rodi's k–ε and the k–ω models, while the SA and SST models yield very good results. As far as the location of this peak vorticity, shown in Figure 6(a), is concerned, all models predict a trajectory that is slightly further away from the wall surface than the measured one, with the discrepancy increasing further downstream. The lateral convection of the vortex is also slightly overestimated. At each streamwise location (Plates 1–4), the value of U is underpredicted in close vicinity of the wall, which may be in part due to underestimation of the cross-stream transfer of momentum by the streamwise vortex developing with downstream distance. Generally, all models appear to produce similar distributions, although Rodi's k–ε model is outperformed by the remaining models in capturing the trends in the turbulence kinetic energy, the y-velocity component, V, and to a lesser extent, the z-velocity component, W.

In summary, the difference between the prediction accuracies of the four turbulence models is not very large. There is consistent evidence, however, that the predictions with Rodi's k–ε model are slightly inferior to those with the remaining models in certain respects. Specifically, all models are capable of capturing the overall rate of diffusion of the streamwise vortex with downstream distance and the trajectory of this vortex, but predictions of the details of the velocity field, hence the extent of cross-stream mass and momentum transfer are not as accurate, with Rodi's k–ε model trailing the other ones in this respect.

Although it is best to base such simulations on an accurate description of the flow non-uniformity at the jet exit plane, such a treatment is not practical since the type of non-uniformity would depend significantly on the jet configuration, the details of the jet pipe and plenum design, as well as the crossflow conditions. For the present approach of specifying

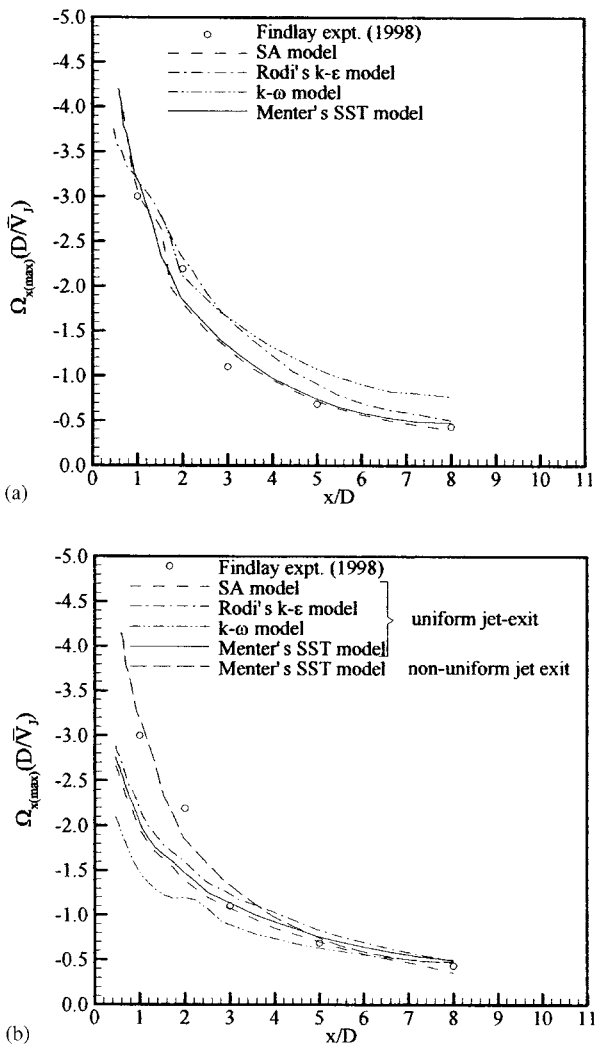

Figure 5. Predicted maximum streamwise vorticity in the jet-induced vorticity field: (a) sensitivity to turbulence models and (b) sensitivity to jet boundary conditions.

inflow boundary conditions at the jet-exit plane to be practical, a more generic distribution must suffice. Sensitivity of the VGJ flow field to this jet boundary condition was therefore tested by comparing predictions with uniform distributions of velocity and turbulence quantities to the original, non-uniform results. The velocity magnitude was adjusted to match the mass flow of the non-uniform case; hence, maintaining the same jet-to-crossflow velocity ratio. As for the non-uniform case, a thin boundary layer ($\delta = 0.16D$) was specified along the perimeter of the jet orifice, so as to avoid sharp velocity gradients that may have triggered solution instability due to excessive levels of shear. An average k value was calculated from the non-uniform distribution and was specified along with a uniform ε value calculated from this value using Equation (1).

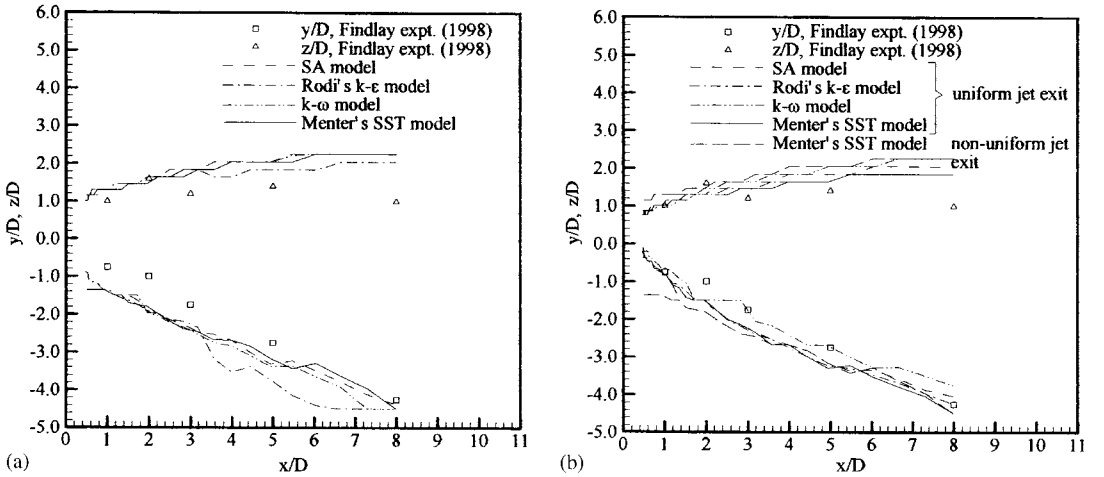

Figure 6. Predicted location of max. streamwise vorticity in the jet-induced vorticity field: (a) sensitivity to turbulence models and (b) sensitivity to jet boundary conditions.

The results with uniform jet-exit conditions are shown in Figures 5(b), 6(b), and with red colour in Plates 1–5. Distinct deviations are noted in these figures from the results with non-uniform treatment of the jet-exit plane. However, these variations are noted to be generally within the margin of error of the simulations with respect to experimental results. It thus appears that uniform boundary conditions may be imposed at the jet-exit plane without notable changes in prediction accuracy when one of the present turbulence models is used. However, it should be noted that this statement is based on tests with a relatively high VR, and there is some evidence that it may not be applicable to lower VR values. For example, Findlay [5] observed higher flow non-uniformity at the jet exit plane with decrease in VR, and Khan [13] noted that the turning of the jet flow was already initiated before leaving the jet hole for a VGJ with VR = 1.0.

3. SIMULATIONS OF THE M2129 DIFFUSING S-DUCT FLOW

The last test case of the present study involves a geometry for a curved diffusing duct that has been used in other published studies to represent the so-called S-duct aircraft engine intake configuration. The M2129 S-duct experiment of Yu [6] was chosen as a reference for the simulations. The M2129 geometry is shown in Figure 7, and key dimensions are given in Tables II and III. The centreline offset and variation of duct diameter with centreline distance are defined in Equations (2) and (3). Parts (a) and (c) of these equations describe extensions upstream and downstream of the original M2129 duct geometry, that were included in the computational domain to simplify the specifications of inflow and outflow boundary conditions.

$$-0.28 \leqslant s/\ell \leqslant 0.00 \quad z_{CL}/\ell = 0 \tag{2a}$$

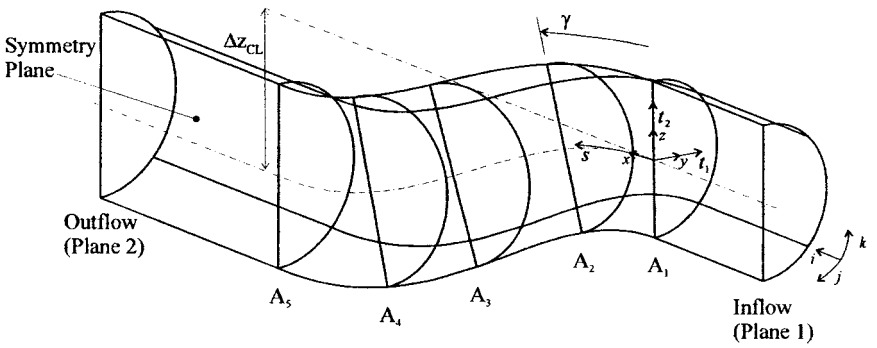

Figure 7. Computational domain for the M2129 diffusing S-duct.

Table II. Location and angle of planes used in data comparison and boundary settings.

Plane	s/ℓ	γ (deg)
Inflow	−0.28	0
A_1	0	0.0*
A_2	0.23	17.6
A_3	0.53	25.1
A_4	0.76	17.7
A_5	1	0
Outflow	1.49	0

*Orientations of all planes are referenced to plane A_1.

Table III. Basic dimensions of the M2129 diffusing S-duct.

$AR = D_2^2/D_1^2$	ℓ/D_1	$\lvert\Delta z_{CL}/\ell\rvert$	ℓ [37]	D_1 [37]
1.4	3.55	0.3	170.4 mm	48 mm

$$0.00 \leqslant s/\ell \leqslant 1.00 \quad \frac{z_{CL}}{\ell} = \frac{\Delta z_{CL}}{2\ell}\left(1 - \cos\left(\pi \frac{s}{\ell}\right)\right) \tag{2b}$$

$$1.00 \leqslant s/\ell \leqslant 1.49 \quad z_{CL}/\ell = \Delta z_{CL}/\ell \tag{2c}$$

$$-0.28 \leqslant s/\ell \leqslant 0.00 \quad D = D_1 \tag{3a}$$

$$0.00 \leqslant s/\ell \leqslant 1.00 \quad \frac{D - D_1}{D_2 - D_1} = 3\left(1 - \frac{s}{\ell}\right)^4 - 4\left(1 - \frac{s}{\ell}\right)^3 + 1 \tag{3b}$$

$$1.00 \leqslant s/\ell \leqslant 1.49 \quad D = D_2 \tag{3c}$$

An apparently more widely used test case for numerical studies of diffusing S-ducts is the M2129 experiments of Willmer *et al.* [14]. Although the geometries employed in both test cases are identical in non-dimensional terms, two important differences exist between them. In Willmer *et al.*'s experiments, inlet Mach numbers of 0.41 and 0.78, and Reynolds numbers (based on inlet velocity and diameter) of 1.16×10^6 and 1.85×10^6 were tested to provide more realistic aircraft flight conditions. Yu's experiments, on the other hand, were performed at an inlet Mach number less than 0.2 and a Reynolds number of 4.3×10^4. Although the flow regime studied by Yu does not quite correspond to a typical aircraft flight condition, inspection of the simulated results of either test case [15, 16] showed them to contain very similar flow features. Since the goal of the present study is to evaluate turbulence model prediction capability of the three-dimensional duct flow field, the differences in Mach numbers and Reynolds numbers do not detract from the suitability of Yu's data as a benchmark. Yu's data was chosen over Willmer *et al.*'s measurements due to the high-resolution of the flow field inside the duct as well as at the duct entrance. Two-component laser-Doppler anemometer measurements of velocity and turbulence were performed in addition to wall static pressure.

3.1. Boundary conditions and iteration parameters

The computational inflow boundary was placed D_1 distance upstream of the beginning of the bent portion of the M2129 S-duct. This allowed specification of unidirectional flow conditions at this boundary. The freestream velocity of 15.4 m/s together with $\rho = 1.2$ kg/m^3 and $\mu = 1.8 \times 10^{-5}$ Pa s at this boundary matched the Reynolds number of Yu's experiments. The inflow freestream k value of 0.36 m^2/s^2 was scaled from Yu's experimental data, and the remaining turbulence properties ($\varepsilon = 16.5$, $\omega = 477$ and $\chi = 44.7$) were estimated based on a dissipation rate calculated as per Equation (1) with D_h replaced by D_1. The radial profiles of streamwise velocity and k in the inflow boundary layer were scaled from experimental data. The k data set was relatively sparse very close to the duct wall; hence, this region was supplemented with simulated flat plate boundary layer data corresponding to a similar value of Re_θ ($= 875$) and freestream turbulence. The boundary-layer profiles of ε, ω and χ were also obtained from these flat plate simulations.

Static pressure was specified at the outflow boundary. A uniform pressure distribution was found to yield better rates of solution convergence than extrapolation of cross-stream pressure gradients from within the domain. The outflow boundary was placed sufficiently downstream of the exit plane of the bend ($1.75D_1$) to prevent this uniform cross-stream pressure specification at the outflow boundary from affecting the natural development of the flow within the bend. Upon convergence with uniform outflow pressure, further iterations with allowance for non-uniform pressures to develop at the outflow boundary did not yield any changes in the flow field within the curved portions of the duct.

For optimum rates of convergence, the artificial compressibility parameter, c/a, was set to $\max[10.0 \text{ m/s}; 3.2V_{\text{local}}]$, while the convective and diffusive time-step limits were determined on the basis of $K_c = 1.8$, $K_d = 0.1$. The artificial dissipation parameter, κ_4, was set to 0.005 as for previous test cases. Initial and lower threshold settings of the turbulence parameters k, ε, ω and χ, were also the same as those used in the previous test cases. The turbulence production-to-destruction ratio ($\mathscr{P}_k/\mathscr{D}_k$) had to be limited to 20 to prevent divergence of the solution with the two-equation models. Furthermore, the k–ω and SST models benefitted from an upper limit that was placed on the eddy viscosity as well. Without this limit,

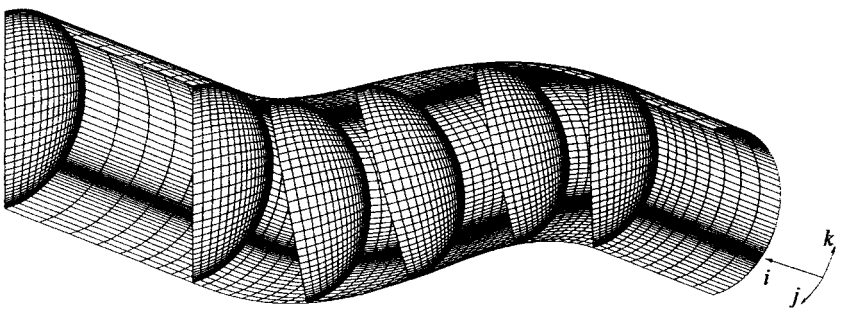

Figure 8. Base grid for the M2129 duct.

localized regions of high eddy-viscosity would tend to appear near the duct walls at various streamwise and circumferential positions during transient development of the flow in pseudo-time. Examination of the converged flow field indicated peak values of μ_e/μ not exceeding 200. Hence, the upper limit setting of $\mu_e/\mu = 350$ did not artificially influence the converged solution.

3.2. Computational grid

In establishing the optimum grid configurations, a base grid ($N_i = 57 \times N_j = 25 \times N_k = 53$) shown in Figure 8, and three other grids that systematically provided local refinement in the cross-stream ($57 \times 31 \times 61$), streamwise ($97 \times 25 \times 53$), and all ($97 \times 31 \times 61$) grid directions were considered. Each grid was generated based on the guidelines established in the simpler test cases that are presented in Part 1 of the paper. At the inflow plane, the first node off the wall was set to $y_1^+ = 1.2$ and 20 nodes were placed within the boundary layer. This type of node distribution at the inflow boundary yielded a minimum number of 15 nodes in the boundary layer and a maximum y_1^+ value of 1.3 anywhere within the duct. The base grid shown in Figure 13 contains significantly fewer nodes than those in published studies on the M2129 duct [16–18], yet simulation results showed that the spatial resolution offered by this grid is sufficient to obtain grid independent results.

As was already noted for the previous test cases, the extent of artificial dissipation affecting the simulation results is a topic that must be addressed in conjunction with optimization of a spatial grid. Comparison of simulation results with values of 0.005 and 0.01 for the scaling coefficient of the dissipation term, κ_4, indicated very small sensitivity to such variations in κ_4 with the finest grid considered, whereas the sensitivity was noticeable with the remaining, coarser grids. Based on the good agreement between the results obtained with all four grids with $\kappa_4 = 0.005$, it appears that this κ_4 value is sufficiently low for all of the grids considered here. Nonetheless, the comparisons of turbulence models presented in the next section are based on the more conservative of the four grids with node counts of $N_i = 97$, $N_j = 31$ and $N_k = 61$.

As with the swirling-flow test case presented in Part 1 of this study, a number of nodes were left out of the computational domain at the two 'corners' of the grid where significant skewness exists. Excluding 7 node $\times$ 7 node segments at these grid corners, as shown in the *computational space* inset of Figure 9, prevented any convergence difficulties. As indicated

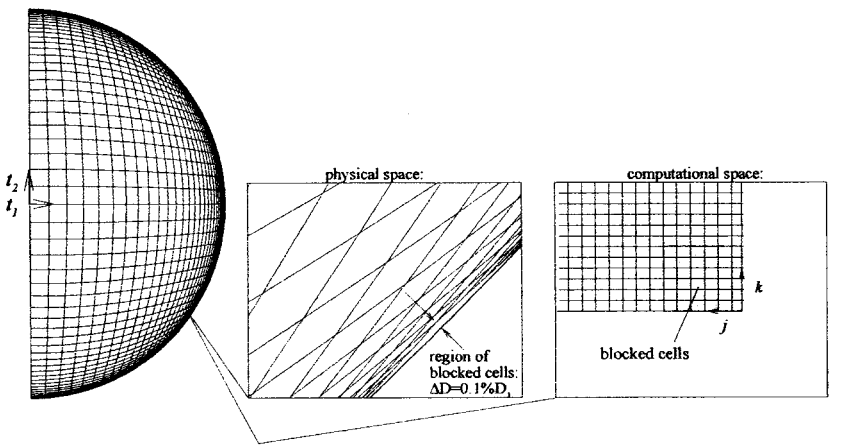

Figure 9. Highly skewed region of the computational grid for the M2129 S-duct.

in the *physical space* inset of the same figure, this resulted in a maximum geometry deviation of 0.1% D_1 from a perfectly circular wall, which is negligibly small. Despite this process of blocking off nodes, there still remained considerable grid skewness at two circumferential positions of the cross-sectional plane. Examination of the simulation results, however, did not indicate any noticeable differences in the boundary-layer structure in these skewed regions compared to elsewhere along the duct perimeter. This result is consistent with the observations in the previously described swirling-flow test case.

3.3. Description a flow physics

This section discusses the physics of the flow, to provide the reader with sufficient background information for the turbulence model comparisons that follow. The important flow features are identified and discussed using results from the SA turbulence model as summarized in Plate 6. As noted in part (b) of this figure, between planes A_1 and A_2 a lobe of positive streamwise vorticity appears adjacent to the side wall ($t_1/D = 0.5, t_2/D = 0.0$). This early stage of the development of a classical streamwise vortex arises from the rotation of the incoming boundary layer vorticity lines due to the flow turning in the first bend. Between this region of positive vorticity and the duct wall, lies a thin layer of negative vorticity attributed to the induced secondary flows. The imposed cross-stream momentum near the wall, producing this sense of wall vorticity, would oppose the generation of secondary flow (which would be of opposite sign) in the second bend. Nonetheless, limited development of such secondary flows is still present in the second bend, as displayed by the vorticity contours in plane A_5 and the outflow plane.

Between planes A_2 and A_5, the lobe of positive vorticity generated in the first bend develops into a well-defined streamwise vortex. The cross-stream convection of this vortex is noted to be consistent with the corresponding induced velocity field near the walls shown in Figure 15(a).

Further insight is gained by examining the vector-field topology through streamline traces next to the duct wall as shown in Figure 10. Between planes A_2 and A_3 such limiting stream-

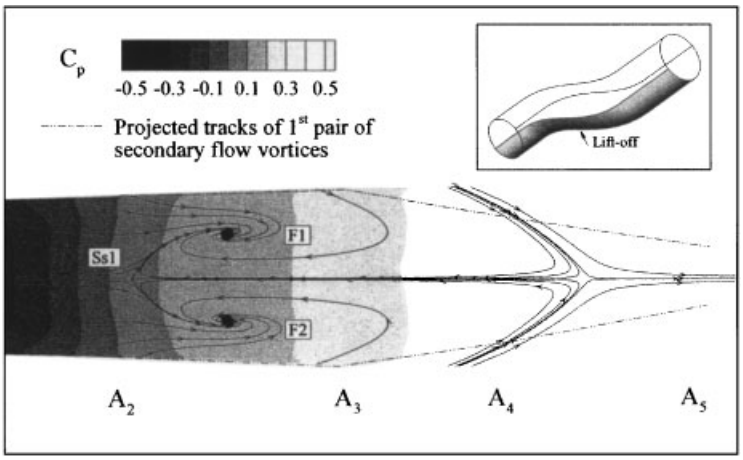

Figure 10. Vortex lift-off in the M2129 diffusing S-duct.

lines are shown to be reoriented from the 'streamwise' direction, briefly pointing upstream and then concentrating into a pair of focus nodes. This phenomenon has been referred to by such authors as Anderson *et al.* [15] as *vortex lift-off*. It may be argued that this flow pattern is the response of the low momentum fluid, swept into this region by the streamwise vortices of the first bend, to the prevailing adverse streamwise pressure gradients. As the streamwise vortex pair continuously feeds low momentum fluid into this region, and this fluid is opposed by pressure forces in the streamwise direction, it lifts off of the surface in the form of a new pair of tornado-like vortices orthogonal to the wall.

Once reoriented in the streamwise direction by the streamwise momentum of the flow further away from the wall, the generated 'lift-off' vortices would have the same sense of rotation as the streamwise vortex pair generated in the first bend, and thus the two vortex pairs most likely merge shortly after lift-off. Evidence of this merging of the vortex pairs is seen in Plate 6(b), where the streamwise vortices of the first bend are noted to loose strength between planes A_2 and A_4, a trend that is reversed between planes A_4 and A_5.

Finally, performance of this diffuser is depicted in Figure 11. The static pressure recovery can be seen to fall far short of the ideal value due to a combination of viscous losses and flow distortion. The development of the pressure loss is fairly gradual with downstream distance, which suggests that the aforementioned lift-off phenomenon and subsequent development of the vorticity field are not significant loss-generation mechanisms in mass-averaged terms.

3.4. Simulation results

For all four turbulence models in question, the predicted streamwise and cross-stream velocity distributions are compared to experimental data in Figures 12–16, and wall static pressure comparisons are given in Figure 17. Due to the availability of experimental data, only the 't_2' component of cross-stream velocity is presented. This should be sufficient to provide an overall indication of the prediction accuracy for the secondary motions in the duct. All four turbulence models are noted to capture the general distribution of velocity reasonably well. It is worth noting that the prediction accuracy of cross-stream motion is better than in the

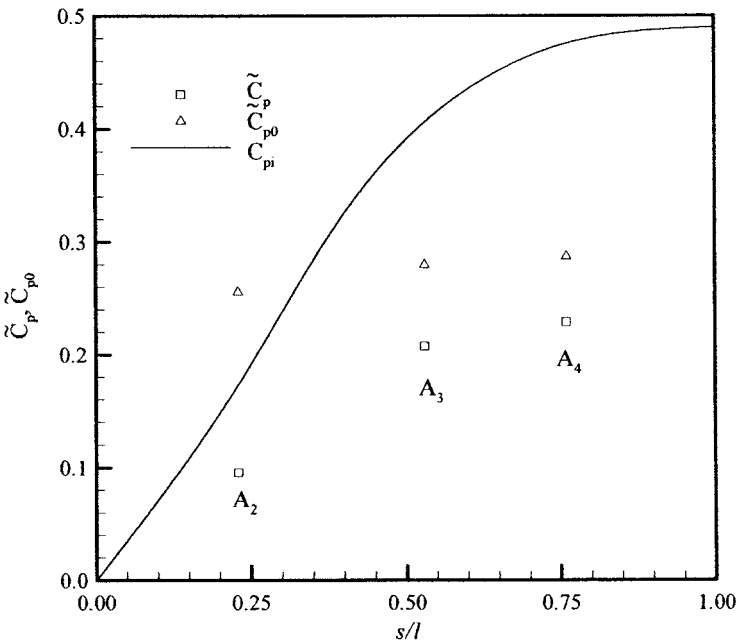

Figure 11. Total pressure losses and static-pressure recovery performance of the M2129 diffusing S-duct.

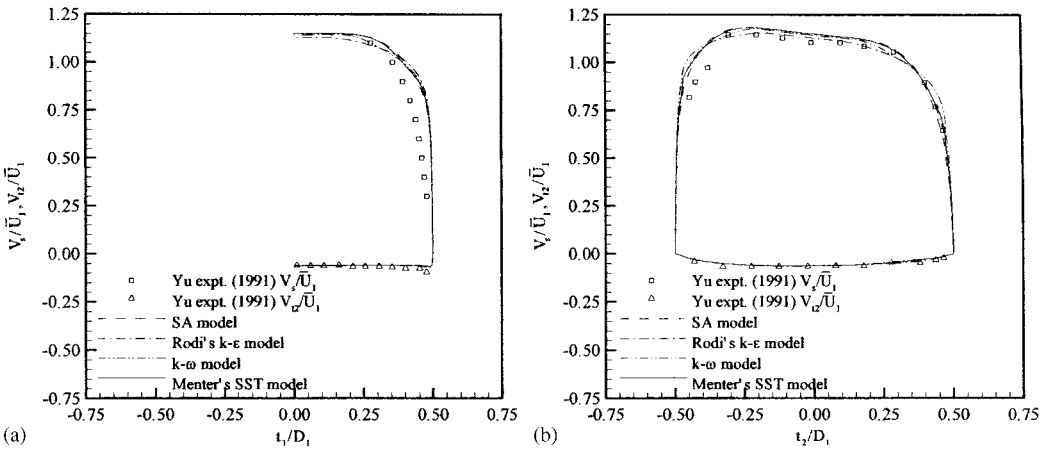

Figure 12. Predictions of the velocity field in Plane A_1 ($s/\ell = 0.0$) compared with the experimental data of Yu (1991): (a) distribution along t_1 and (b) distribution along t_2.

strongly swirling flow of So *et al.* considered in Part 1 of this study. This may be due to the weaker swirl and the strong role of cross-stream pressure gradients in the development of the secondary motion in the S-duct, in contrast with the strongly swirling, shear driven flow of So *et al.* As for the streamwise velocity distribution, the one area where all four models are in mutual agreement, yet fail to follow the experimental trend, is along the side portion

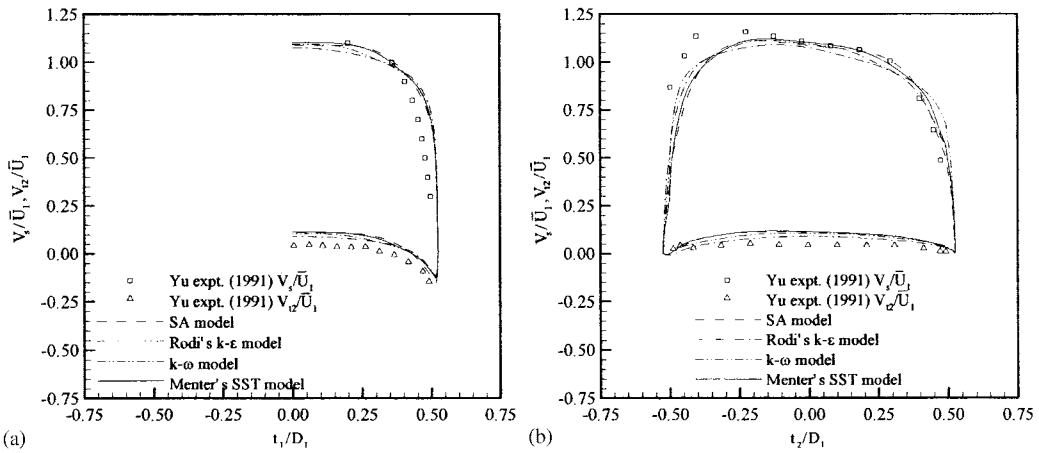

Figure 13. Predictions of the velocity field in Plane A_2 ($s/\ell = 0.24$) compared with the experimental data of Yu [6]: (a) distribution along t_1 and (b) distribution along t_2.

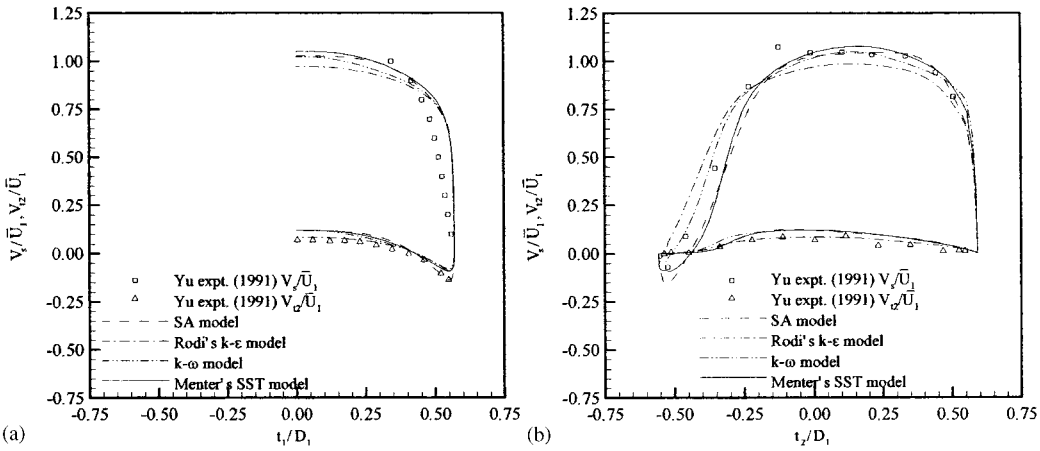

Figure 14. Predictions of the velocity field in plane A_3 ($s/\ell = 0.54$) compared with the experimental data of Yu [6]: (a) distribution along t_1 and (b) distribution along t_2.

of the duct ($t_1 = D/2, t_2 = 0$). The measured V_s distribution at this location is indicative of a notably thicker streamwise boundary layer than the predicted ones, and this trend is persistent at all five cross-stream planes. This discrepancy may be the combined result of the accuracy with which the streamwise pressure gradient is predicted along the walls (Figure 17) as well as the prediction accuracy for the cross-stream motion, since both of these factors influence the streamwise momentum of the local flow.

The variations amongst the turbulence models do not appear to be substantial with the exception of the region of vortex lift-off and further downstream of this region, as observed

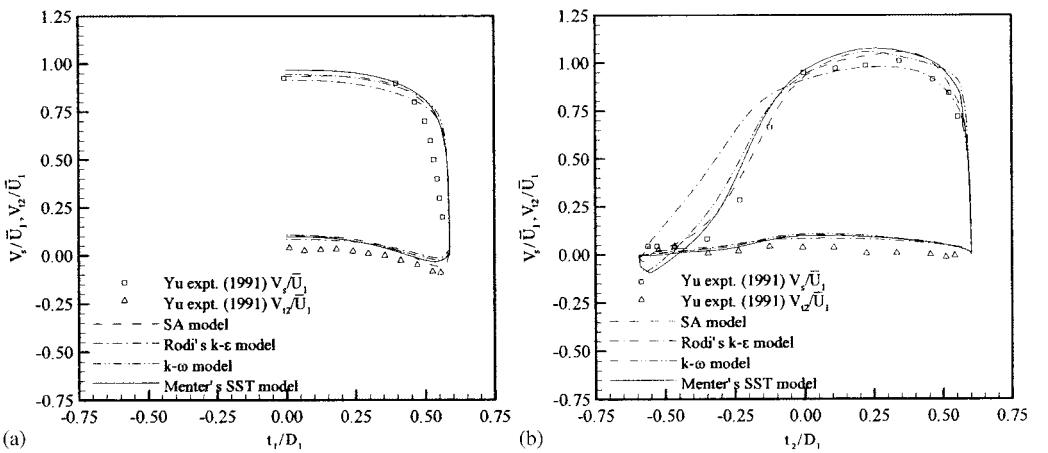

Figure 15. Predictions of the velocity field in plane A_4 ($s/\ell = 0.76$) compared with the experimental data of Yu [6]: (a) distribution along t_1 and (b) distribution along t_2.

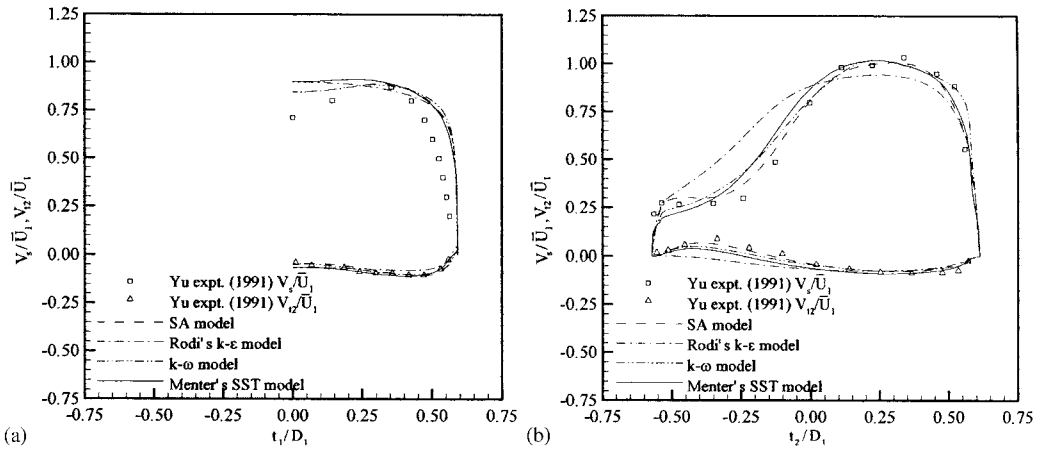

Figure 16. Predictions of the velocity field in plane A_5 ($s/\ell = 1.0$) compared with the experimental data of Yu [6]: (a) distribution along t_1 and (b) distribution along t_2.

in the comparisons within planes A_3, A_4 and A_5. Particularly, Rodi's k–ε model is noted to be consistently outperformed by the remaining turbulence models in this portion of the duct.

The wall static pressure distributions at the 'top', 'bottom' and 'side' of the duct (Figure 17) display a generally acceptable agreement between the predictions and experimental data. Amongst the four turbulence models, the prediction of Menter's SST model is noted to be consistently more accurate at all three circumferential positions. The relatively poor performance of Rodi's k–ε model is consistent with the model's lesser ability in capturing the vortex lift-off about half-way through the duct.

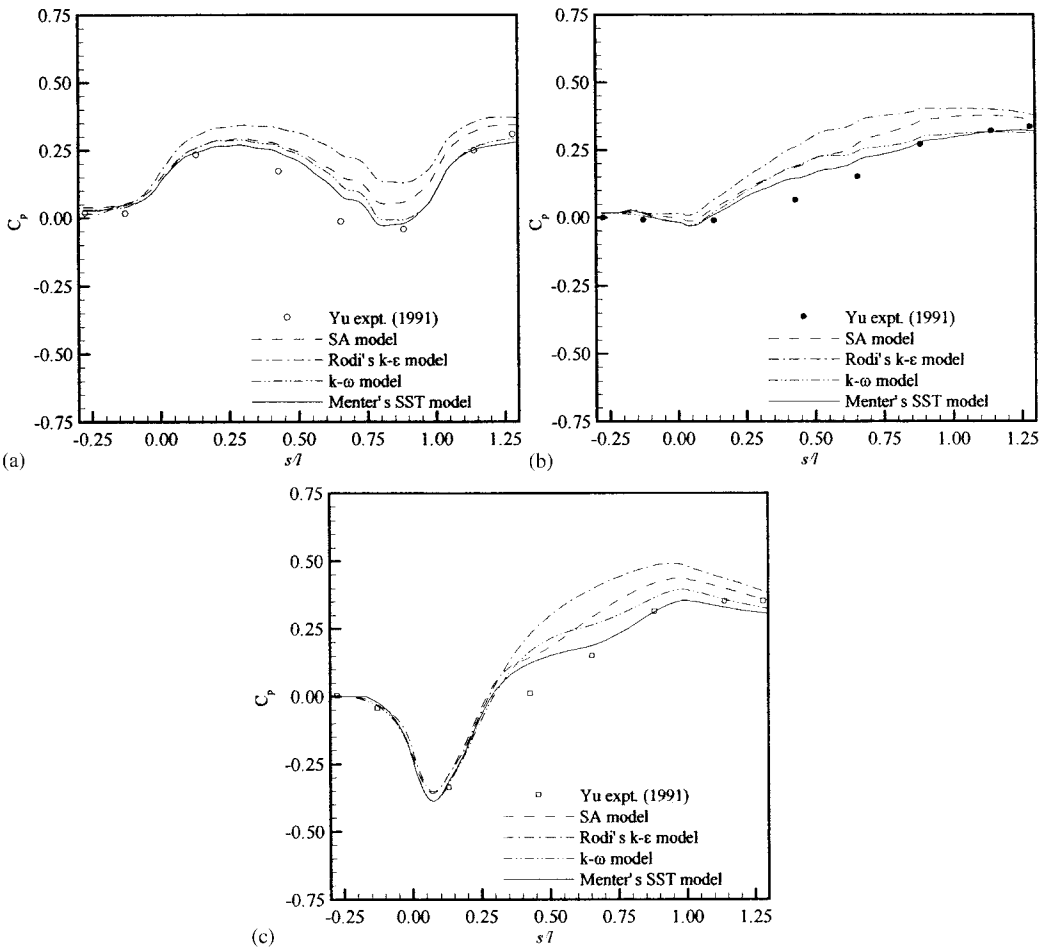

Figure 17. Predicted wall static pressure compared with the experimental data of Yu [6]: (a) streamwise distribution along $t_1 = 0$, $t_2 = D/2$, (b) streamwise distribution along $t_1 = D/2$, $t_2 = 0$ and (c) streamwise distribution along $t_1 = 0$, $t_2 = -D/2$.

4. CONCLUSIONS

The two-layer k–ε model of Rodi [1], the k–ω model of Wilcox [2], the two-equation shear–stress-transport model of Menter [3], and the one-equation eddy-viscosity model of Spalart and Allmaras [4] were further evaluated for complex three-dimensional flows, based on near-wall spatial resolutions that were established in Part 1 of this study. The following main observations are drawn:

- Simulations were performed for a periodic (VGJ) flow of 30° pitch, 90° skew, a jet-to-crossflow velocity ratio of 1.5, and an approach boundary-layer thickness of about twice

the streamwise dimension of the jet orifice (D). For this configuration, node counts of 47, 37 and 29 in the streamwise, spanwise and vertical directions were found to be sufficient to yield essentially grid-independent results with the computational domain being $13D$ long, $5D$ high and $3D$ wide. Accounting for the flow non-uniformity at the jet orifice inflow boundary was found to have a noticeable effect on the prediction accuracy. However, the extent of this effect was observed to be comparable to the typical difference between measured data and predictions based on any one of the turbulence models considered.

- The difference between the prediction accuracies of the four turbulence models (Rodi's k–ε, Menter's SST, k–ω, and SA) in the VGJ flow was not very significant. However, the predictions with Rodi's k–ε model were noted to be consistently less accurate than with the remaining models in certain respects. Specifically, all four models were able to reproduce the rate of diffusion of the streamwise vortex with downstream distance and the trajectory of this vortex reasonably well, but predictions of the overall velocity field, hence the extent of cross-stream mass and momentum transfer were not as accurate, with Rodi's k–ε model trailing the other models in this respect.
- The second test case was based on a diffusing S-duct, with a geometry that is typical of a longitudinally curved aircraft engine intake. Grid optimization studies revealed that nearly grid independent results were achievable based on approximately 1400 nodes in the cross-stream plane and about 60 nodes in the streamwise direction, with any one of the four turbulence models. All four models were able to capture the overall streamwise and secondary flow development reasonably well. Rodi's k–ε model was noted to be particularly less accurate in the region of vortex lift-off. This observation is consistent with the results in the VGJ flow, where vortex lift-off just downstream of the jet orifice is also a key feature of the overall flow development.
- Considering all of the test cases examined in Parts 1 and 2 of this study, the one-equation model of Spalart and Allmaras [4] is found to provide the best combination of: minimum resolution requirements of wall boundary layers, consistent prediction accuracy, robustness and computational efficiency.

A byproduct of the present study is the evaluation of a particular Navier–Stokes algorithm for three-dimensional separated flows. It has been demonstrated that iterative solution of the Navier–Stokes equations through alternating implicit/explicit pseudo-time marching based on two-stage *Runge–Kutta* integration, combined with local sizing of pseudo-time steps and a multigrid procedure as acceleration schemes, is an efficient and robust algorithm for such flows. Additionally, explicit control over artificial dissipation terms facilitated by the algorithm has been shown to be very effective in being able to suppress the development of spurious spatial oscillations, without introducing excessive numerical diffusion into the solution that would undermine the predictive capability of the turbulence models. Finally, the capability of a certain type of preconditioning of the mass and momentum equations to allow monotonic and efficient convergence in the incompressible regime has been demonstrated, and appropriate settings for the relevant preconditioning parameters have been provided.

NOMENCLATURE

$a_1 \ldots a_4$	constants used in scaling the preconditioning parameter, c
AR	diffuser outlet-to-inlet area ratio
c	parameter used in the preconditioning of Q in the $\partial Q/\partial t_p$ term
C_f	skin friction coefficient $(=\tau_w/(1/2\rho_{ref} V_{ref}^2))$
C_p	static pressure coefficient
C_{p0}	total pressure coefficient
D	duct diameter; streamwise dimension of jet-exit hole
D_h	hydraulic diameter
$\mathscr{D}_k$	rate of destruction of turbulence kinetic energy
i, j, k	node indices in the ξ, η, ζ grid directions
K_c, K_d	constants used in determining the convective and diffusive pseudo-time-step limits
k	turbulence kinetic energy (m^2/s^2)
ℓ	length of M2129 diffusing S-duct along centreline
N_i, N_j, N_k	number of nodes in the i, j and k grid directions, respectively
$\mathscr{P}_k$	rate of production of turbulence kinetic energy
Q	vector of conservation variables
Re	Reynolds number
Re_θ	Reynolds number based on momentum thickness
s	streamwise distance; distance along centreline
t_1, t_2	curvilinear co-ordinates associated with crossflow plane in the S-duct
t_p	pseudo-time
U	x-velocity component
V	velocity vector; y-velocity component
V_j	jet velocity
$\bar{V}_j$	area-averaged jet velocity
V_{local}	local velocity magnitude (m/s)
V_s	velocity component in the streamwise (s) direction (m/s)
V_t	cross-stream (tangential) velocity component
V_{t2}	velocity component in the t_2 direction
VGJ	vortex-generator jet
VR	jet-to-crossflow velocity ratio
W	z-velocity component
x, y, z	Cartesian co-ordinates
$\kappa^{(2)}$, $\kappa^{(4)}$	constants used in calculation of artificial dissipation
δ	boundary layer thickness
θ	vectored-jet skew angle from crossflow direction
Φ	vectored-jet-in-crossflow pitch angle from surface
γ	orientation of crossflow planes in the diffusing S-duct
$\tilde{\nu}_e$	eddy-viscosity variable used in the Spalart–Allmaras turbulence model
μ	dynamic viscosity
μ_e	dynamic eddy viscosity
χ	$\dfrac{\tilde{\nu}_e}{\nu}$

ρ	density
ω	specific dissipation rate of turbulence kinetic energy (s^{-1})
Ω	magnitude of vorticity
ε	dissipation rate of turbulence kinetic energy (m^2/s^3)

Subscripts

ref	reference quantities used for non-dimensionalization
CL	centreline

ACKNOWLEDGEMENTS

The research presented herein was undertaken with the financial support of National Research Council of Canada under contract no. 31184-8-8847/001/ST. The co-operation of Drs I. S. Gartshore and M. J. Findlay in making their experimental data on the inclined-jet-in-crossflow available is also acknowledged.

REFERENCES

1. Rodi W. Recent developments in turbulence modeling. In *Proceedings of the 3rd International Symposium on Refined Flow Modeling and Turbulence Measurements*, Iwasa Y, Tamai N, Wada A (eds), Tokyo, Japan, 1988.
2. Wilcox DC. *Turbulence Modeling for CFD* (2nd edn). DCW Industries: La Cañada, CA, 1988.
3. Menter FR. Eddy viscosity transport models and their relation to the $k-\varepsilon$ model. *NASA Technical Memorandum* TM-108854, 1994.
4. Spalart PR, Allmaras SR. A one equation turbulence model for aerodynamic flows. *AIAA Paper 92-0439*, 1992.
5. Findlay M. An experimental and numerical investigation of inclined jets in a crossflow. *Ph.D. Thesis*, University of British Columbia, Canada, 1998.
6. Yu C-M. Flow characteristics in S-shaped diffusing ducts. *Ph.D. Thesis*, Imperial College, University of London, U.K., 1991.
7. Hassan I, Findlay M, Salcudean M, Gartshore I. Prediction of film cooling with compound-angle injection using different turbulence models. *Proceedings of CFD'98*, CFD Society of Canada, 1998; x1–x6.
8. Kim S-W, Benson TJ. Fluid flow of a row of jets in crossflow—a numerical study. *AIAA Journal* 1993; **31**: 806–811.
9. Henry FS, Pearcey HH. Numerical model of boundary-layer control using air-jet generated vortices. *AIAA Journal* 1994; **32**:2415–2425.
10. Alvarez J, Jones WP, Seoud R. Predictions of momentum and scalar fields in a jet in cross-flow using first and second order turbulence closures. *AGARD-CP-534*, 1993; 24-1–24-10.
11. Zhang X. Interaction between a turbulent boundary layer and elliptic and rectangular jets. In *Proceedings of the 2nd International Symposium on Engineering Turbulence Modelling and Experiments*, *Florence*, vol. 2, Rodi W, Martelli F (eds), 1993; 251–260.
12. Barberopoulos AA, Garry KP. The effect of skewing on the vorticity produced by an airjet vortex generator. *The Aeronautical Journal* 1998; 171–177 (Paper No. 2275).
13. Khan ZU. On the dominant vortex created by a pitched and skewed jet in crossflow. *Ph.D. Thesis*, Stanford University, 1999.
14. Willmer AC, Brown TW, Goldsmith EL. Effects of intake geometry on circular pitot intake performance at zero and low forward speeds. *AGARD CP301*, Toulouse, France, 1981.
15. Anderson BH, Reddy DR, Kapoor K. A comparative study of full Navier–Stokes and reduced Navier–Stokes analyses for separating flows within a diffusing inlet *S*-duct. *AIAA Paper 93-2154*, 1993.
16. Lee KM, Yu SCM. Computational studies of flows in the RAE 2129 S-shaped diffusing duct. *AIAA Paper 94-0658*, 1994.
17. Anderson BH, Gibb J. Application of computational fluid dynamics to the study of vortex flow control for the management of inlet distortion. *AIAA Paper 92-3177*, 1992.
18. Marquis AJ, Ong LY. The computation of flow in a RAE M2129 diffuser using low Reynolds number $k-\varepsilon$ turbulence models. *Proceedings of Ninth International Conference on Numerical Methods in Laminar and Turbulent Flows*, *Atlanta, GA*, 1995; 841–851.

